Gyrokinetic particle simulation of drift-compressional modes in dipole geometry

Peter Porazik[a] and Zhihong Lin[b]
Department of Physics and Astronomy, University of California, Irvine, California 92697, USA

(Received 14 January 2011; accepted 2 June 2011; published online 21 July 2011)

Gyrokinetic particle simulation of low frequency compressional modes has been developed using flux coordinates in the global magnetic dipole geometry. The compressional component is formulated in a scalar form of the parallel magnetic perturbation, and the gyro-averaging is performed explicitly in the configuration space. A reduced gyrokinetic model, in which the compressional perturbations are decoupled from the shear Alfvén and electrostatic perturbations, has been implemented. Linear simulation results have been verified using a numerical Nyquist analysis of the dispersion relation in the slab limit. Global simulations of unstable drift-compressional modes in the dipole geometry with kinetic ions find that finite Larmor radius (FLR) effects reduce the linear growth rate significantly but change little the real frequency. Global eigenmode structures show that the modes are even along the equilibrium magnetic field and broadened by the FLR effects in the radial direction. Radial propagation away from the region of excitation is observed.
 [doi:10.1063/1.3605031]

I. INTRODUCTION

Ultra low frequency (ULF) waves are regularly observed in the Earth's magnetosphere. Often, similar ULF waves are observed under different magnetospheric conditions, which suggests that waves with similar characteristics may in fact be manifestation of different physical mechanisms.[1] Ideally, the physical mechanism responsible for a particular observation may be determined by considering whether the source of the wave energy is an external drive (e.g., the solar wind) or an internal excitation via phase space or configuration space nonuniformities and whether the energy is released by reactive or dissipative processes. The physical mechanism used to explain the observations of the internally excited compressional Pc 5 (period of $\sim 150-600$ s) waves[2–4] is commonly that of the drift-mirror mode.[5] Drift-mirror modes are compressional modes which derive their energy from temperature anisotropy and whose energy is released by wave-particle interactions[6] (collisionless dissipative processes).

A particular observation of a compressional Pc 5 wave may be attributed to drift-mirror modes if the instability threshold for these modes is crossed. If this is not the case, an alternative explanation should be found. It has been shown[7] that one alternative explanation could be drift-compressional modes, similar to the magnetic trapped particle modes.[8] Various forms of drift-compressional modes in the geotail flux tubes were analysed in Ref. 9, and a systematic analytic study has been performed in Ref. 10 by carrying out nonlocal eigenmode stability analysis along the field line and addressing coupling to shear Alfvén waves as well as effects of the finite Larmor radius (FLR).

A thorough understanding of the linear and nonlinear properties of drift-compressional modes on a global scale is necessary in order to compare the theory to satellite observations. The central problems in the linear regime are the instability threshold, eigenmode structures in parallel (along the magnetic field) and radial directions, and the possibility of coupling to other modes such as the kinetic shear Alfvén wave. In the nonlinear regime, the main issues are saturation mechanisms, the wave-induced loss-cone, and transport of energetic particles.

Previous investigations were mostly done in simple equilibria, rarely addressing issues like global eigenmode structure or the effects of trapped particles and finite Larmor radius. Due to the complicated geometry of the realistic magnetospheric equilibrium and the importance of kinetic effects, a complete analytic study of the drift-compressional modes on the global scale is difficult even in the linear regime. An efficient method to resolve these difficulties is computer simulation based on first-principles formulation. Furthermore, to self-consistently investigate the effects of trapped particles, finite Larmor radius and linear as well as nonlinear wave-particle interaction, it is necessary to work in the domain of kinetic rather than fluid theory.

This paper describes the development and verification of a global gyrokinetic particle-in-cell simulation code in a dipole geometry to study the ULF drift-compressional modes. The compressional component has been formulated in terms of the parallel magnetic perturbation $\delta B_{\parallel}$. A numerical scheme has been devised for gyrokinetic simulations of low frequency compressional modes, in which gyro-averaging is performed explicitly in configuration space. The particle simulation code has been designed using the field-aligned flux coordinates for efficient representation of the magnetic dipole geometry. The code has been verified in the slab limit using numerical Nyquist analysis of a slab dispersion relation. Linear gyrokinetic simulations were performed

[a]Electronic mail: pporazik@uci.edu.
[b]Author to whom correspondence should be addressed. Electronic mail: zhihongl@uci.edu.

to investigate the effects of the kinetic ions and finite Larmor radius on the frequency and growth rate. FLR effects were observed to decrease the growth rate of the unstable mode but change little the real frequency. Simulations were also conducted to resolve, for the first time, the global structure of the eigenmode both in the radial direction and along the equilibrium magnetic field. The parallel mode structure was found to be even. Broadening of radial structure was observed when FLR effects were included. Analysis of time evolution of the radial structure shows radial propagation away from the region of excitation.

Section II describes some general features of the theoretical model on which the simulation code was founded and discusses a formulation for compressional magnetic perturbations and the dipole flux coordinates. In Sec. III A the model is reduced to purely compressional magnetic perturbations. The simulation code for this model is described in Sec. III B. A linear verification against a dispersion relation in a slab limit is presented in Sec. III C. Section III D discusses some linear properties of the drift-compressional mode obtained from the global simulation. Summary is given in Sec. IV. Appendices A and B contain more detailed discussions of the gyrokinetic simulation model presented in Secs. II and III.

II. FORMULATION OF GYROKINETIC SIMULATION IN DIPOLE GEOMETRY

A. Gyrokinetic system for compressible electromagnetic modes

The full gyrokinetic system should describe multitude of low frequency waves, such as ion acoustic waves, drift waves, shear Alfvén waves, and slow magnetoacoustic waves, in order to investigate effects such as linear and nonlinear mode coupling. The waves of interest satisfy $\omega/\Omega_i \sim O(\delta)$, $k_\parallel \rho_i \sim O(\delta)$, $\rho_i|\nabla \ln B_0| \equiv \rho_i/L_B \sim O(\delta)$, and $k_\perp \rho_i \sim O(1)$, where ω is the wave frequency, $\Omega_i = eB_0/m_i c$ is the ion cyclotron frequency, $\rho_i = \sqrt{T_i/m_i}/\Omega_i$ is the Larmor radius, $k_\perp$ and $k_\parallel$ are wave vectors perpendicular and parallel to the magnetic field, and $\delta \ll 1$ is a small parameter. It is therefore valid and appropriate to employ the gyrokinetic theory. Following Refs. 11, 12, the gyrokinetic Vlasov equation, which governs the evolution of $F(\mathbf{X}, v_\parallel, \mu)$, may be written as

$$\partial_t F + \dot{\mathbf{X}} \cdot \nabla F + \dot{v}_\parallel \partial_{v_\parallel} F = 0, \tag{1}$$

where F is the gyrocenter distribution function averaged over the fast gyro-motion and $(\mathbf{X}, v_\parallel, \mu)$ is a set of gyrocenter variables standing for gyrocenter position $\mathbf{X}$, parallel velocity $v_\parallel$, and magnetic moment μ, respectively (Appendix A). Since μ is an adiabatic invariant, the term $\dot{\mu}\partial_\mu F$ does not appear. The gyrocenter equations of motion are, to first order,[11,13]

$$\dot{\mathbf{X}} = v_\parallel\left(\widehat{\mathbf{b}} + \frac{\delta \mathbf{B}_\perp}{B_0}\right) + \frac{\widehat{\mathbf{b}}}{m\Omega} \times \left(\mu B_0 \nabla \ln B_0 + m v_\parallel^2 \widehat{\mathbf{b}} \cdot \nabla \widehat{\mathbf{b}}\right) + \frac{c}{B_0}\widehat{\mathbf{b}} \times \nabla\left(\langle\delta\Phi\rangle - \langle\delta\mathbf{A}_\perp \cdot \frac{\mathbf{v}_\perp}{c}\rangle\right), \tag{2}$$

$$\dot{v}_\parallel = -\frac{e}{mc}\frac{\partial\langle\delta A_\parallel\rangle}{\partial t} - \frac{e}{m}\left(\widehat{\mathbf{b}} + \frac{\langle\delta\mathbf{B}_\perp\rangle}{B_0}\right) \cdot \nabla\langle\delta\Phi\rangle - \frac{1}{m}\left(\widehat{\mathbf{b}} + \frac{\langle\delta\mathbf{B}_\perp\rangle}{B_0}\right) \cdot \nabla\left(\mu B_0 - e\langle\delta\mathbf{A}_\perp \cdot \frac{\mathbf{v}_\perp}{c}\rangle\right) - \frac{c v_\parallel}{B_0}\widehat{\mathbf{b}} \times \left(\widehat{\mathbf{b}} \cdot \nabla\widehat{\mathbf{b}}\right) \cdot \nabla\left(\langle\delta\Phi\rangle - \langle\frac{\mathbf{v}_\perp}{c} \cdot \delta\mathbf{A}_\perp\rangle\right), \tag{3}$$

where $\delta\mathbf{B} = \nabla \times \delta\mathbf{A}$ and $\widehat{\mathbf{b}}$ is the unit vector pointing along the equilibrium magnetic field at the particle position. The $\langle\ldots\rangle$ stands for the gyro-phase average performed by the operation $\frac{1}{2\pi}\oint \ldots\, d\xi$, where ξ is the gyro-phase angle. Physically, the first term on the right hand side of Eq. (2) is the parallel velocity along the total magnetic field, the second term contains the equilibrium curvature and gradient-B magnetic drifts, and the third term contains the perturbed $E \times B$ drift and the perturbed magnetic drifts. In Eq. (3), the first two terms on the right hand side represent the parallel acceleration due to the perturbed electric field, the third term contains the parallel acceleration due to total mirror force, and the last term is of higher order but is important for phase space conservation.[11]

The perturbed densities and currents in real space are found from

$$\delta\rho(\mathbf{x}) = \sum q \int \delta f(\mathbf{x}, \mathbf{v}) d\mathbf{v}, \tag{4}$$

$$\delta\mathbf{J}(\mathbf{x}) = \sum q \int \mathbf{v}\delta f(\mathbf{x}, \mathbf{v}) d\mathbf{v}. \tag{5}$$

The perturbed particle distribution function $\delta f = f - f_0$ in particle phase space $(\mathbf{x}, \mathbf{v})$ is related to the perturbed gyrocenter distribution function $\delta F = F - F_0$ by

$$\delta f(\mathbf{x}, \mathbf{v}, t) = \delta F - \frac{e}{T} F_0\{\delta\Phi - \langle\delta\Phi\rangle + \langle\delta\mathbf{A} \cdot \mathbf{v}_\perp/c\rangle\}, \tag{6}$$

where f_0 and F_0 are particle and gyrocenter equilibrium distribution functions, respectively (Appendix A). The system is closed using the Poisson's equation and the Ampère's law, assuming $k_\parallel \ll k_\perp$,

$$\nabla_\perp^2 \delta\Phi(\mathbf{x}) = -4\pi\delta\rho(\mathbf{x}), \tag{7}$$

$$\nabla_\perp^2 \delta\mathbf{A}(\mathbf{x}) = -\frac{4\pi}{c}\delta\mathbf{J}(\mathbf{x}). \tag{8}$$

More detailed discussion of the system, which also includes temperature anisotropy, is presented in Appendix B.

B. Formulation for compressional magnetic perturbations

In the gyrokinetic theory, the fundamental operation of gyro-phase averaging reduces the number of dynamical variables from six, in the particle phase space $(\mathbf{x}, \mathbf{v})$, to five in the gyrocenter phase space $(\mathbf{X}, v_\parallel, \mu)$. This, in turn, results in the decrease of the number of independent field quantities appearing in the Maxwell's equations. Thus, the perpendicular Ampère's law has now only one degree of freedom. It is then undesirable to use $\delta \mathbf{A}_\perp$ rather than $\delta B_\parallel$ in gyrokinetic simulation of the compressional modes,[6] since $\delta B_\parallel$ is a scalar and a more physical and fundamental field quantity than $\delta \mathbf{A}_\perp$. Adopting the convention of Ref. 14, the independent quantities are the electrostatic potential $\delta\Phi$, the parallel component of the vector potential $\delta A_\parallel$, and the compressional component of the magnetic perturbation $\delta B_\parallel$. In the current work,[15] a gyrokinetic system for low frequency compressional modes in general geometry is expressed fully in terms of the compressional component of the magnetic perturbation $\delta B_\parallel$. This introduces a "gyro-surface" average of $\delta B_\parallel$ in the gyrocenter equations of motion and similarly in the perpendicular Ampère's law, which takes the form of the low frequency perpendicular force balance equation.[11,16] The gyrocenter response to the electromagnetic field $\delta B_\parallel$ is fully contained in the $\langle \delta \mathbf{A}_\perp \cdot \mathbf{v}_\perp \rangle$ term of Eqs. (2) and (3), which may be expressed in terms of $\delta B_\parallel$ using the Stoke's theorem as

$$\langle \delta \mathbf{A}_\perp \cdot \mathbf{v}_\perp \rangle = -\Omega_i \left\langle \int_0^\rho \delta B_\parallel r dr \right\rangle = -\frac{c}{e}\mu \langle\langle \delta B_\parallel \rangle\rangle, \quad (9)$$

where $\langle\langle ... \rangle\rangle \equiv \frac{1}{\pi\rho^2}\int_0^{2\pi}\int_0^\rho ...\, r dr d\xi$ is the gyro-surface average, with r being the gyro-radius integration variable, and $\rho = v_\perp/\Omega_i$. Similarly, the perpendicular Ampère's law, when cast into the form of the perpendicular low frequency force balance equation, using Eq. (A10) in Appendix A and the Stoke's theorem in the perpendicular component of Eq. (8), becomes

$$\frac{\delta B_\parallel B_0}{4\pi} + 2\pi\Omega_i^2 \int d\mu dv_\parallel \left(B_0 \left\langle \int_0^\rho \delta F r dr \right\rangle + \frac{F_0}{\rho_i^2} \left\langle \int_0^\rho \left\langle \int_0^\rho \delta B_\parallel r' dr' \right\rangle r dr \right\rangle \right) = 0, \quad (10)$$

where $T_\parallel = T_\perp$ has been assumed and only ions are considered, removing the sum over particle species for simplicity. The first term is the perturbed magnetic pressure, which is balanced by the perturbed particle pressure. The perturbed particle pressure consists of a perturbed gyrocenter pressure (the second term) and another component (the third term) arising from the coordinate transformation between gyrocenter and particle coordinates. The origin of this additional component is the perpendicular current from the imbalance between ion and electron $\mathbf{E}_\perp \times \mathbf{B}$ drifts due to the ion FLR effects.[17,18] Here $\mathbf{E}_\perp = -c^{-1}\partial_t \mathbf{A}_\perp$ is the inductive electric field from the first time derivative of the perpendicular vector potential $\mathbf{A}_\perp$. The second time derivative of $\mathbf{A}_\perp$, which gives rise to the fast magnetoacoustic wave,[19] has been dropped as a result of frequency ordering.

A formal expression of Eq. (9) may be obtained using an operator representation to write $\delta B_\parallel(\mathbf{x}, t) = \delta B_\parallel e^{i\mathbf{r}\cdot\mathbf{k}_\perp}$, with $\mathbf{k}_\perp = -i\nabla_\perp$. Then Eq. (9) may be written as

$$\langle \delta \mathbf{A}_\perp \cdot \mathbf{v}_\perp \rangle = -\frac{c}{e}\mu \frac{2}{k_\perp \rho} J_1(k_\perp \rho)\delta B_\parallel. \quad (11)$$

Similarly, using $e^{-i\mathbf{r}\cdot\mathbf{k}_\perp}$ to move back to particle phase space, Eq. (10) may be formally written as[11]

$$\frac{\delta B_\parallel B_0}{4\pi} + 2\pi \int \mu B_0 \left(\frac{2}{k_\perp \rho} J_1(k_\perp \rho) \right) \delta F \frac{B_0}{m} dv_\parallel d\mu + \frac{\beta}{4\pi}\left[I_0\left((k_\perp \rho_i)^2 \right) - I_1\left((k_\perp \rho_i)^2 \right) \right] e^{-(k_\perp\rho_i)^2} \delta B_\parallel B_0 = 0, \quad (12)$$

where I_0 and I_1 are the 0th and 1st order modified Bessel functions, respectively. It should be noted that in deriving the scalar form of the perpendicular Ampère's law (Eq. (10) and Eq. (12)) it was assumed that $\delta\Phi = 0 = \delta A_\parallel$, electrons are cold, and the ion equilibrium is described by an isotropic Maxwellian. A more complete derivation of the force balance equation, with nonzero $\delta\Phi$ and $\delta A_\parallel$, appears in Eq. (B10) of Appendix B.

In the perturbed gyrocenter equations of motion (Eqs. (2) and (3)), the $\delta B_\parallel$ is averaged over the gyro-surface with a gyro-radius of ρ in Eq. (9). For perturbations with $k_\perp \rho_i \lesssim 3$, it has been demonstrated[15] that it is sufficient to approximate the surface integral using the gyro-phase averaging technique, similar to Ref. 20, but at an effective gyro-radius of $\rho/\sqrt{2}$. This is schematically illustrated in Figure 1, where $J_0(k_\perp\rho)$ stands for the usual gyro-phase averaging, $2J_1(k_\perp\rho)/k_\perp\rho$ stands for gyro-surface averaging, and $J_0(k_\perp\rho/\sqrt{2})$ stands for the gyro-orbit averaging at the effective radius of $\rho/\sqrt{2}$ as the approximation of the gyro-surface averaging. In addition, the magnetic moment integral in Eq. (10) may be approximated by carefully choosing samples in the μ-coordinate and their corresponding weights.[15,21]

C. Flux coordinates for dipole geometry

It is convenient to use the flux coordinates (χ, ψ, ζ), in which the field lines are straight. The flux coordinates are defined by $\mathbf{B}_0 = \nabla\psi \times \nabla\zeta$, where ψ and ζ represent two directions perpendicular to the equilibrium magnetic field $\mathbf{B}_0$. This coordinate system is aligned with the magnetic field lines, because the covariant base vector corresponding to the third coordinate χ points along the magnetic field $\mathbf{B}_0$, i.e., $\mathbf{B}_0 = J^{-1}\partial_\chi \mathbf{r}$. Also, in this coordinate system the magnetic

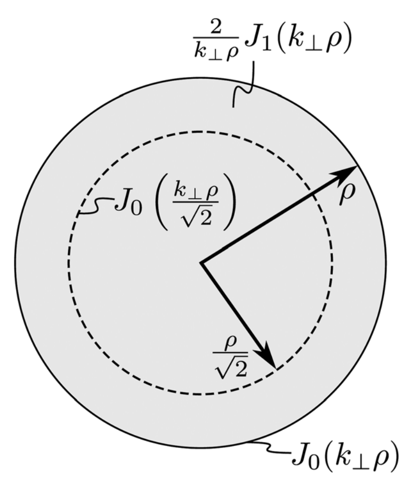

FIG. 1. The average over the surface (shaded area) enclosed by the gyro-orbit (solid line), which appears in Eq. (9), may be approximated by averaging over a gyro-orbit with an effective radius of $\rho/\sqrt{2}$ (dashed circles).

field lines are straight, and the coordinates ψ and ζ are field line labels since $\mathbf{B}_0 \cdot \nabla\psi = 0$ and $\mathbf{B}_0 \cdot \nabla\zeta = 0$.

A self consistent magnetospheric equilibrium is an extremely complex system. However, at distances of up to approximately 6 Earth radii, which includes the plasmasphere, the equilibrium magnetic field is approximately that of an ideal magnetic dipole.[22,23] The magnetic field of the ideal dipole in spherical coordinates (r, θ, ϕ), with θ measured from the positive z-axis, is $\mathbf{B}_0 = M(2\cos\theta\hat{r} + \sin\theta\hat{\theta})/r^3$, where M is the magnetic dipole moment. The magnetic dipole moment of the Earth is approximately 8.6×10^{25} gauss cm^3.

From the expression for the ideal dipole, the transformation equations between the flux coordinates and the spherical coordinates were chosen such that $\chi = \theta$, $\psi = M\sin^2\theta/r$, and $\zeta = \phi$. The coordinate χ is similar to the geomagnetic latitude, the coordinate ψ is the flux function, and the coordinate ζ is the symmetric coordinate along the azimuthal direction. This choice results in a nonorthogonal coordinate system with the contravariant metric tensor, $g^{\alpha\beta} = \nabla\alpha \cdot \nabla\beta$,

$$g^{\alpha\beta} = \frac{1}{M^2}\begin{pmatrix} \frac{\psi^2}{\sin^4\chi} & \frac{2\psi^3\cos\chi}{\sin^5\chi} & 0 \\ \frac{2\psi^3\cos\chi}{\sin^5\chi} & \frac{\psi^4(3\cos^2\chi+1)}{\sin^6\chi} & 0 \\ 0 & 0 & \frac{\psi^2}{\sin^6\chi} \end{pmatrix}, \qquad (13)$$

and the Jacobian $J = M^3\sin^7\chi/\psi^4$. The coordinate system is illustrated in Figure 2.

More realistic dipole models,[24,25] which include the lowest order correction in β, do not dramatically alter the qualitative features of the ideal dipole model, where β is the ratio of plasma kinetic pressure to magnetic pressure. In such dipole models, the flux coordinates would still be a good choice for simulation.

D. Gyro-orbit averaging in flux coordinates

The Larmor radius vector $\boldsymbol{\rho}$ is orthogonal to a flux surface ψ. Thus, given the gyrocenter position (χ, ψ) at some azimuthal angle, finding the particle position ρ away from the gyrocenter, involves finding the change in both coordinates $(\Delta\chi, \Delta\psi)$. The Larmor radius vector $\boldsymbol{\rho}$ is perpendicular to the equilibrium magnetic field line and can therefore be expressed as $\boldsymbol{\rho} = \rho_\psi\nabla\psi + \rho_\zeta\nabla\zeta$. The relationship of the Larmor radius vector to the coordinate grid is illustrated in Figure 3 on the $\chi - \psi$ plane. If the Larmor radius is small compared to the gradient scale length of the Jacobian,

$$\begin{aligned} \Delta\chi &\approx \rho_\psi g^{\psi\chi}, \\ \Delta\psi &\approx \rho_\psi g^{\psi\psi}, \\ \Delta\zeta &\approx \rho_\zeta g^{\zeta\zeta}. \end{aligned} \qquad (14)$$

since $\boldsymbol{\rho} \cdot \nabla\alpha = \rho^\alpha = g^{\beta\alpha}\rho_\beta$. The metric tensor $g^{\alpha\beta}$ is given in Eq. (13). In the case of 4-point averaging, the expressions for ρ_α only need to be found at the 4-points over which the gyrophase average is performed. Two of the 4-points may be chosen to be along the azimuthal direction, at points for which $\rho_\chi = \rho_\psi = 0$, and the other two at points for which $\rho_\zeta = 0$. Since $\rho^2 = \boldsymbol{\rho} \cdot \boldsymbol{\rho} = g^{\alpha\beta}\rho_\alpha\rho_\beta$, for the case that $\rho_\psi = 0$, it is found that $\rho_\zeta^2 = \rho^2/g^{\zeta\zeta}$. Similarly, for the case that $\rho_\zeta = 0$, it is found that $\rho_\psi^2 = \rho^2/g^{\psi\psi}$. By combining this with Eq. (14), the following expressions are obtained:

$$\begin{aligned} \Delta\chi &\approx \rho\frac{g^{\psi\chi}}{\sqrt{g^{\psi\psi}}}, \\ \Delta\psi &\approx \rho\sqrt{g^{\psi\psi}}, \\ \Delta\zeta &\approx \rho\sqrt{g^{\zeta\zeta}}. \end{aligned} \qquad (15)$$

The nonorthogonality of the coordinate system is reflected in nonzero $\Delta\chi$. If the Larmor radius is small compared to the parallel wavelength of the perturbation, then this difference is also small and may be ignored. If $k_\perp\rho_i \lesssim O(1)$, then this condition may be related to the $k_\parallel/k_\perp \ll 1$ ordering.

III. GLOBAL GYROKINETIC PARTICLE SIMULATION OF DRIFT-COMPRESSIONAL MODES

A. Reduced model for purely compressional magnetic perturbations

The reduced model for drift-compressional modes assumed $\omega/k_\parallel v_A \ll 1$, where $v_A = B_0/\sqrt{4\pi n_0 m_i}$ is the

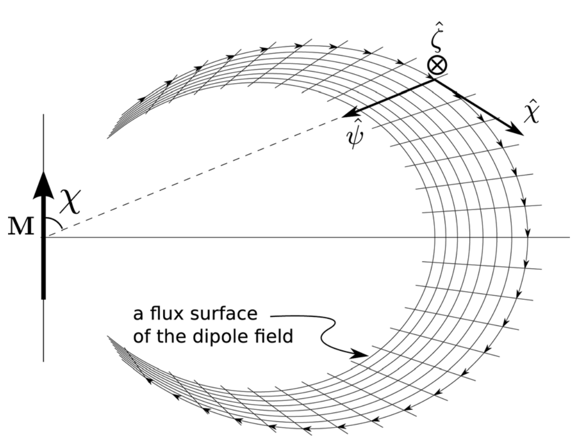

FIG. 2. Flux coordinates (χ, ψ, ζ) for a dipole magnetic field. $\vec{M}$ stands for the magnetic dipole moment, which points in the direction of the large arrow at the dipole center. The small arrows on the outer flux surface indicate the direction of the magnetic field.

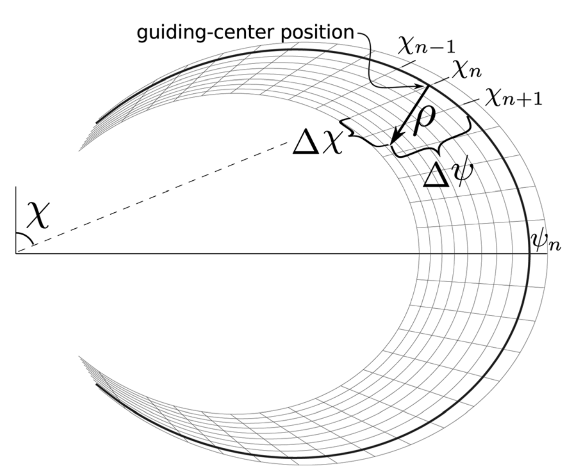

FIG. 3. Gyro-orbit averaging in the flux coordinates. The relationship of the Larmor radius vector to the coordinate grid in the $\chi - \psi$ plane.

Alfvén speed, in order that the compressional mode is decoupled from the shear Alfvén wave.[10] The electrons are assumed cold and do not contribute to the kinetic pressure, but short out the parallel electric field so that $\delta\Phi = 0$, i.e., ion acoustic wave is removed.[10] Since the focus is on the drift-compressional modes, the temperatures are assumed to be isotropic $T_{i\parallel} = T_{i\perp}$, which removes the drift-mirror instability from consideration. The simulation model thus consists of the gyrokinetic equation for ions and the low frequency perpendicular force balance equation, given in Eqs. (10). Using Eqs. (1)–(3), and (9), the gyrokinetic equation in the flux coordinates may be written as

$$(\partial_t + \dot{\chi}\partial_\chi + \dot{\psi}\partial_\psi + \dot{\zeta}\partial_\zeta + \dot{v}_\parallel\partial_{v_\parallel})F = 0, \tag{16}$$

or $\frac{d}{dt}F \equiv (\partial_t + \dot{\mathbf{Z}}\cdot\partial_{\mathbf{Z}})F = 0$, where the gyrocenter equations of motions are given by

$$\dot{\chi} = \frac{B_0}{B_\chi}v_\parallel + \frac{B_\psi}{B_\chi}\frac{c}{e}\mu\partial_\zeta\langle\langle\delta B_\parallel\rangle\rangle, \tag{17}$$

$$\dot{\psi} = -\frac{c}{e}\mu\partial_\zeta\langle\langle\delta B_\parallel\rangle\rangle, \tag{18}$$

$$\dot{\zeta} = \frac{c}{e}\left(mv_\parallel^2 + \mu B_0\right)\left(\partial_\psi - \frac{B_\psi}{B_\chi}\partial_\chi\right)\ln B_0 + \frac{c}{e}\mu\left(\partial_\psi - \frac{B_\psi}{B_\chi}\partial_\chi\right)\langle\langle\delta B_\parallel\rangle\rangle, \tag{19}$$

$$\dot{v}_\parallel = -\frac{B_0}{B_\chi}\frac{\mu}{m}\partial_\chi B_0 + v_\parallel\dot{\psi}\left(\partial_\psi - \frac{B_\psi}{B_\chi}\partial_\chi\right)\ln B_0 - \frac{B_0}{B_\chi}\frac{\mu}{m}\partial_\chi\langle\langle\delta B_\parallel\rangle\rangle. \tag{20}$$

The quantities B_χ and B_ψ are covariant components of the equilibrium magnetic field $\mathbf{B}_0 = B_\chi\nabla\chi + B_\psi\nabla\psi$,

$$B_\chi = \frac{\psi^2}{M}(1 + 3\cos^2\chi)\csc^5\chi,$$
$$B_\psi = -\frac{2\psi}{M}\cot\chi\csc^3\chi.$$

The terms in the equations of motion containing B_ψ/B_χ are due to the nonorthogonality of the coordinate system.

The linearization of Eq. (16), using $F = F_0 + \delta F$, yields

$$\begin{aligned}(\partial_t &+ \dot{\chi}_0\partial_\chi + \dot{\zeta}_0\partial_\zeta + \dot{v}_{\parallel 0}\partial_{v_\parallel})\delta F \\ &= \frac{c\mu}{eT_0(\psi)}F_0\left(\frac{B_\psi}{B_\chi}\partial_\chi\ln B_0 - \partial_\psi\ln B_0\right)\left(mv_\parallel^2 + \mu B_0\right)\partial_\zeta\langle\langle\delta B_\parallel\rangle\rangle \\ &+ \frac{c}{e}\mu F_0\partial_\psi\ln n_0(\psi)\left(1 - \frac{3}{2}\eta + \frac{1}{T_0(\psi)}\left[\frac{mv_\parallel^2}{2} + \mu B_0(\chi,\psi)\right]\right) \\ &\times\partial_\zeta\langle\langle\delta B_\parallel\rangle\rangle - \frac{B_0}{B_\chi}\frac{\mu v_\parallel F_0}{T_0(\psi)}\partial_\chi\langle\langle\delta B_\parallel\rangle\rangle. \end{aligned}\tag{21}$$

Eqs. (21) and (10) form a closed system. The equilibrium guiding-center distribution function (Ref. 26), F_0, is assumed to be a local Maxwellian

$$F_0 = n_0(\psi)\sqrt{\frac{m^3}{(2\pi T_0(\psi))^3}}e^{-\left(\frac{1}{2}mv_\parallel^2 + \mu B_0(\chi,\psi)\right)/T_0(\psi)}$$

and $\eta = \partial_\psi\ln T_0(\psi)/\partial_\psi\ln n_0(\psi)$. Since Eq. (18) contains no equilibrium terms, the equilibrium drift is only in the azimuthal direction. Guiding-centers thus never drift away from their initial flux surface. This is due to the azimuthal symmetry of the dipole field. The guiding-center equilibrium distribution function then automatically satisfies $\frac{d}{dt}\big|_0 F_0 = 0$, where $\frac{d}{dt}\big|_0 \equiv \partial_t + \dot{\mathbf{Z}}_0\cdot\partial_{\mathbf{Z}}$ signifies the equilibrium total time derivative operator and $\dot{\mathbf{Z}}_0$ are the unperturbed equations of motion. As is commonly done in perturbative fusion simulations,[27] the equilibrium force balance is assumed to be satisfied *a priori* by the solution of the equilibrium guiding-center distribution function F_0.

B. Global gyrokinetic particle code in dipole geometry

Since the waves of interest are internally excited by wave-particle interactions, the particle simulation was used. Particle simulations also allow for natural treatment of trapped particle and FLR effects. Furthermore, for N simulation particles, the particle-in-cell technique[28] reduces the number of operations per time step from $O(N^2)$ to $O(N\log N)$ by introducing a computational grid on which the fields are solved and interpolated to particle positions. In effect the simulation particle has a finite size, which depends on its interpolation function, also known as the shape function. This also reduces the discrete particle noise.[28] The computational grid in the simulation code is three dimensional and aligned to the dipole field using the flux coordinates (χ, ψ, ζ). The shape function is linear, i.e., the contribution of each particle to a grid point of an enclosing cell is determined by the fraction of the particles volume within that cell.

The gyrokinetic equation is solved using the δf-method,[29,30] in which all the simulation particles are used to represent only the perturbed gyrocenter distribution function δF, resulting in reduced particle noise as compared to full F simulations. The method is similar to analytic integration along characteristics for the equilibrium F_0. The phase space of particles is sampled. Each phase space sample, or volume element, is called a marker particle. A state of a marker particle is defined by its position, velocity, and weight. The weight of a marker particle represents its relative contribution to δF and is defined by $w_j \equiv \frac{\delta F}{F}\big|_{\mathbf{z}=\mathbf{z}_j}$, where $\mathbf{z}$ represents a set of phase space variables and j labels one of the N marker particles. The time evolution of the weight function is determined[29] by

$$\frac{d}{dt}w_j = -(1 - w_j)\frac{d}{dt}\ln F_0. \tag{22}$$

Further details can be found in Refs. 20, 29. Linearization of Eq. (22) yields

$$\frac{d}{dt}w_j = -\frac{d}{dt}\ln F_0, \tag{23}$$

where $w_j \equiv \frac{\delta F}{F_0}\big|_{\mathbf{z}=\mathbf{z}_j}$. Equation (23) was used in linear simulations of this paper.

The equations of motion are integrated in time using the second order Runge–Kutta algorithm. To increase the computational capability of the simulation code to treat a large number of particles, the code has been parallelized using open specifications for multiprocessing (OpenMP).

C. Linear verification in slab limit

Linear simulations were run for the parameters which were identified to be unstable for the compressional modes, and the frequencies and growth rates were compared with the numerically obtained results. Figure 4 shows the scan of the η parameter in the drift-kinetic limit, i.e., $k_\perp \rho_i \to 0$. In these simulations, the simulation domain was set to approximate the slab, i.e., the radial range was much smaller than the simulation radius r and the poloidal (χ) boundaries were close to the equator. In addition, the boundary conditions were set to be periodic, and only the lowest mode number was kept. The density profile used in the equilibrium distribution function, F_0, was modeled using $n_0 = N\left(-\tanh\left(\left[r - \left(r_{\max} - \frac{\Delta r}{2}\right)\right] d\right) + 2\right)$, where $r = K/\psi$ is the equatorial distance from the Earth in units of Larmor radius at $r_{\max}$, $r_{\max}$ is the equatorial distance to the end of the simulation domain, Δr is the equatorial width of the simulation domain, d is the ratio of the width of the sharp drop of density to the total width of the simulation domain, N is a constant related to the density at the maximum equatorial distance, and K is the normalization constant. The tanh function models regions of sharp drop in density, as in the plasmapause. The temperature profile was determined using the parameter η and $T_i = T n_0^\eta$, where T is a constant related to the temperature at the maximum equatorial distance of the simulation. The simulations were performed with approximately 3×10^6 particles, 110 particles per cell, 33 grid points along the field line, 16 grid points in the azimuthal direction, 50 grid points in the $\nabla\psi$ direction, and time step of 10 Ω_i^{-1}. The temperature was $T_i = 0.3$ KeV, $\beta = 14.5$, maximum simulation radius was 1440 ρ_i, radial range was 158 ρ_i, χ-range was 0.15rads, and azimuthal mode number was $n = 1700$. The cyclotron frequency at the maximum simulation radius was $\Omega_i \approx 4.2\text{s}^{-1}$, and Larmor radius was $\rho_i \approx 40$km. Additionally, $\rho_i/L_B \approx 0.002$ which establishes that the plasma is magnetized and $k_\parallel/k_\perp \approx 0.014$. The measurements were taken at the equator and a radial location of $1364\rho_i$. The figure shows simulation results for seven different η values. Although the only parameter changed between the simulations was η, the parameters $k_\parallel v_{ti}$, ω_*, ω_D, and β had to be determined from their radial profiles, which are functions of η.

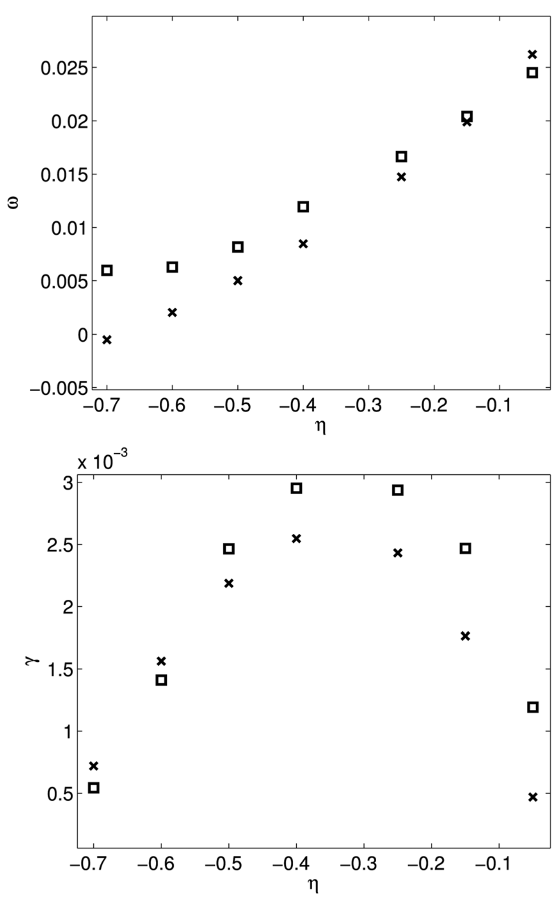

FIG. 4. Variation of frequency ω and growth rate γ, in units of Ω_i, with parameter η as obtained from gyrokinetic particle simulation ($\square$), and from numerical Nyquist analysis ($\times$) in the slab limit. FLR effects are ignored.

The simulation results were compared to an analytic dispersion relation. In the slab limit, the model for the reduced drift-compressional mode leads to the linear dispersion relation

$$1 + \frac{\beta}{(\kappa_\perp \rho_i)^2}\left\{\left[\omega - \omega_*\left(1 - \frac{3}{2}\eta\right)\right]K_1 - \omega_* \eta K_2\right\} = 0, \tag{24}$$

where $\beta = 8\pi n_0 T_i/B_0^2$, $v_{ti} = \sqrt{T_i/m_i}$, $\omega_D = k_\perp v_D = k_\perp \frac{cT_i}{eB_0}\partial_x \ln B_0$, $\omega_* = k_\perp v_* = k_\perp \frac{cT_i}{eB_0}\partial_x \ln n_0$, $\eta = \frac{\partial_\psi \ln T_i(x)}{\partial_\psi \ln n_0(x)}$, $k_\perp \to k_y$, x is along the equator increasing radially outward, y is in the uniform (azimuthal) direction, and

$$K_1 = \frac{1}{\sqrt{\pi}}\int_0^\infty \int_{-\infty}^\infty \frac{\epsilon J_1^2(\sqrt{2}k_\perp \rho_i \sqrt{\epsilon}) e^{-\epsilon - \xi^2}}{\omega - \omega_D \epsilon - \xi\sqrt{2} v_{ti} k_\parallel} d\xi d\epsilon,$$

$$K_2 = \frac{1}{\sqrt{\pi}}\int_0^\infty \int_{-\infty}^\infty \frac{\epsilon J_1^2(\sqrt{2}k_\perp \rho_i \sqrt{\epsilon})(\epsilon + \xi^2) e^{-\epsilon - \xi^2}}{\omega - \omega_D \epsilon - \xi\sqrt{2} v_{ti} k_\parallel} d\xi d\epsilon,$$

in which $\epsilon = \frac{\mu B_0}{T_i}$, $\xi = \frac{v_\parallel}{\sqrt{2} v_{ti}}$, and J_1 is the first order Bessel functions of the first kind. The dispersion relation (24) was solved using numerical Nyquist analysis.

Figure 4 shows that the effect of η on frequency and growth rate from simulation is qualitatively very similar to that from Nyquist analysis of the slab dispersion relation. The results for frequency agree better for higher values of η, while the results for growth rate agree better for lower values of η. The maximum growth rate, however, is approximately at the same location. The slight discrepancies are attributed to the differences between the dipole geometry in which the particle-in-cell simulation was performed, and the slab geometry in which the analytic dispersion relation was obtained.

The simulation code has been extended to the gyrokinetic regime to study the FLR effect on the frequency and growth rate. The initial results were obtained in the limit that

$k_\psi/k_\zeta \ll 1$. In this limit, the formal expression (Eqs. (11) and (12)) may be implemented to take the FLR into account. Figure 5 shows the verification of these modifications against the numerical Nyquist analysis of the slab dispersion relation given by Eq. (24). The value of $k_\perp\rho_i$ was scanned independently of the azimuthal mode number n, which was held fixed. The quantitative agreement improves as $k_\perp\rho_i$ approaches the value of 1. As $k_\perp\rho_i$ is increased, the frequency slightly increases, while growth rate decreases more dramatically.

D. Linear properties of drift-compressional mode in dipole geometry

In order to resolve the unstable structure along the equilibrium field, the poloidal simulation domain was extended to the global dipole geometry. The modifications to the simulation code required considerations of the boundary conditions of the perturbed magnetic field $\delta B_\parallel$ and the marker particles. For the perturbed magnetic field, it was required that at the χ boundaries $\delta B_\parallel = 0$. This is equivalent to assuming that the ionosphere at these boundaries behaves as a perfect conductor. The boundary condition of the marker particles is reflective. This is accomplished by changing the direction of the parallel velocity of the particle when it crosses either of the boundaries. The effective reflection of the particle is equivalent to letting one particle enter the simulation domain for each particle that leaves the domain. The boundary conditions in the ψ direction only enter through gyro-averaging operators, i.e., when FLR effects are considered. In such cases, it is assumed that the field does not change appreciably across the boundary. In addition, the equilibrium gradients are chosen to be negligible in the vicinity of the ψ-boundaries. The azimuthal (ζ) boundary conditions are periodic. The simulations are initialized by assigning small random weight, w_i, to each marker particle, thus reproducing random low amplitude noise.

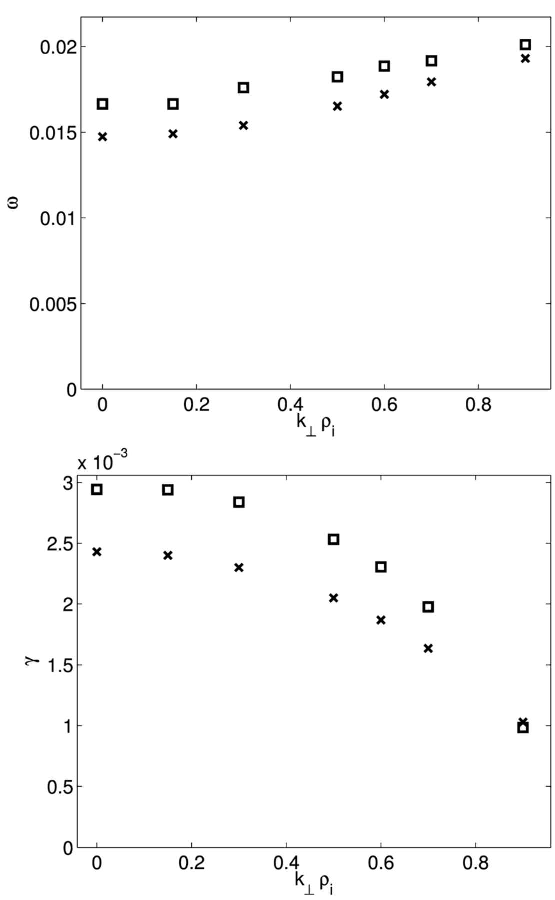

FIG. 5. Finite Larmor radius effects on frequency ω and growth rate γ, in units of Ω_i, as obtained from gyrokinetic particle simulation (□), and from numerical Nyquist analysis (×) in slab limit.

In order to observe how the χ-domain size (along parallel direction) affects the frequency and growth rate, it has been varied from 1 to 2.2 radians centered at the equator. In all cases the wave frequency and growth rate were unchanged, being of value $0.1257\Omega_i$ and $0.0047\Omega_i$, respectively. The wave propagation was in the direction of ion magnetic drift. The change of the field-aligned structure of the magnetic field perturbation due to the variation of the χ-domain is presented in Figure 6, in which $\delta B_\parallel$ is plotted in the $\chi - \psi$ plane at a particular time. It can be seen from the figure that past 1.8 radians, the size of the χ-domain, has no effect on the field-aligned mode structure. This can be regarded as the convergence study for the parallel simulation domain. The mode is even and localized around the equator due to strong magnetic field near the polar regions. These simulations were performed in the drift-kinetic limit, i.e., $k_\perp\rho_i \to 0$.

To verify the explicit gyro-averaging in the equations of motion as described in Sec. II B, $\Delta\psi = \Delta\chi = 0$ was first imposed in Eq. (15), which amounts to explicitly enforcing the $k_\psi/k_\zeta \to 0$ limit, and compared to results obtained using Bessel functions. Thus, at first, only 2-points along the ζ coordinate were used to perform the gyro-average. The results showed instability of frequency $0.044\Omega_i$ and growth rate of $0.0023\Omega_i$. With Bessel functions, the frequency was $0.044\Omega_i$ and growth rate was $0.0024\Omega_i$, being in good agreement. 4-point averaging was next implemented by determining $\Delta\chi$, $\Delta\psi$ as well as $\Delta\zeta$ from Eq. (15). The frequency in this case was $0.044\Omega_i$, same as with 2-point averaging, and as in the drift-kinetic limit. However, while the growth rate

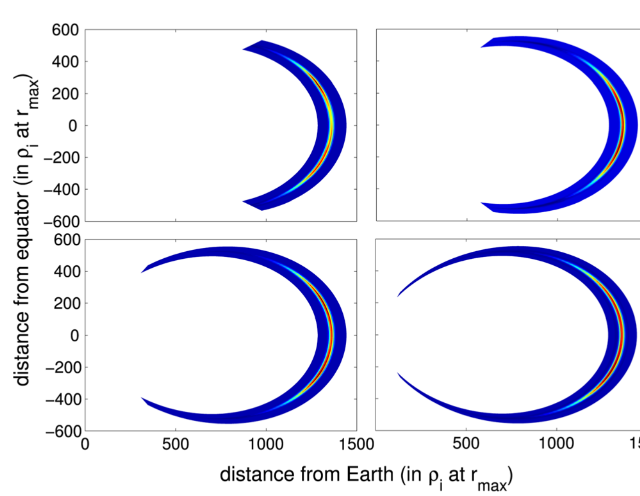

FIG. 6. (Color) Simulation results for field-aligned structures of $\delta B_\parallel$, obtained from simulations having different χ-domain sizes. The χ-range for the case shown in the upper left corner is 1 radians, upper right corner is 1.4 radians, lower left corner is 1.8 radians, and lower right corner is 2.2 radians.

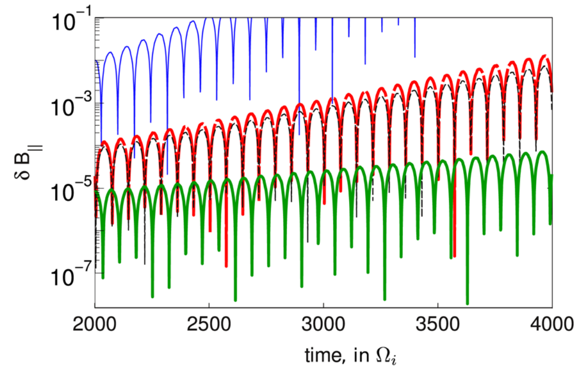

FIG. 7. (Color online) Time evolution of $\delta B_{\|}$ on the equatorial plane, at the radial location corresponding to largest amplitude, from the drift-kinetic simulation (blue, thin, solid line), gyrokinetic simulation using Bessel functions with $k_\perp = k_\zeta$ (red, thick, interrupted line), gyrokinetic simulation using 2-points along ζ (black, thin, interrupted line), and gyrokinetic simulation using 4-point averaging to approximate the gyro-surface average (green, thick, solid line).

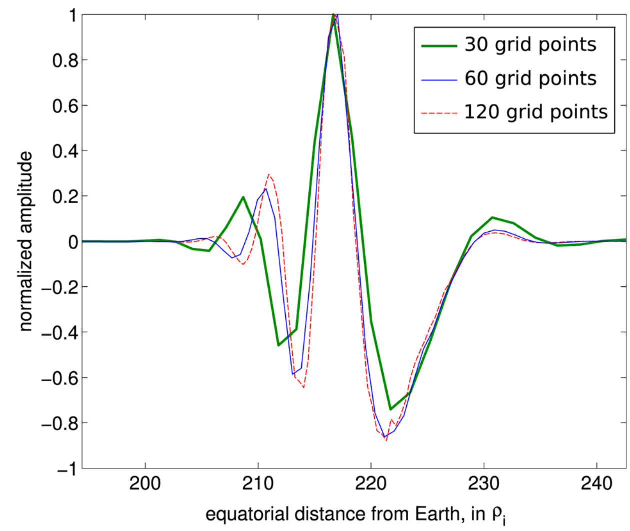

FIG. 9. (Color online) Convergence study of the radial structure of $\delta B_{\|}$. The case with 30 grid points in the radial direction is represented by the green, thick, solid line; the case with 60 grid points is represented by the blue, thin, solid line; and the case with 120 grid points is represented by the red, thin, interrupted line. 4-point gyro-averaging was used in the equations of motion.The measurement was taken at the equator.

in the drift-kinetic limit was $0.0048\Omega_i$, with 4-point averaging it decreased to $0.0011\Omega_i$. These results are summarized in Fig. 7. The simulation parameters in all of the shown cases were $T_i = 84.5$ KeV, $\beta = 13.68$, $\eta = -0.25$, $r_{max} = 9.1$ Earth radii, or about $82\rho_i$, and the azimuthal mode number was $n = 50$ so that $k_\zeta \rho_i \approx 0.9$.

Following these tests, more consistent gyrokinetic simulations were performed by estimating $k_\perp^2$ in the low frequency force balance equation as $k_\psi^2 + k_\zeta^2$. Figures 8 and 9 are convergence studies with respect to the number of particles and the number of grid points in the radial direction. The top panel of Fig. 8 shows that it is sufficient to use approximately 2.2×10^6 particles. To obtain the bottom panel of Fig. 8, the simulation was run with 30, 60, and 120 grid points in the radial direction, using 2.2×10^6 marker particles, and a point along the equator was chosen at which the frequency and growth rate were measured. The figure shows that the frequency does not change when this parameter is varied; the growth rate changes only slightly when the number of grid points is changed from 30 to 60 and does not change when it is increased to 120. The dependence of radial structure on the number of grid points is shown in Fig. 9. All three simulations showed approximately the same structure, but the results with 60 and 120 grid points show closest agreement.

Building on the code verification and convergence study, physical results of a gyrokinetic simulation in global dipole geometry whose profile is given in Fig. 10 were investigated. Figure 11 shows a contour plot of $\delta B_{\|}$ in the $\chi - \psi$ plane at a particular time towards the end of simulation in which the temperature at $r_{\max}$ was $T_i = 8.45$KeV, $\beta = 13.68$, $\eta = -0.6$, and azimuthal mode number was $n = 250$. Other parameters described in Sec. III C, which

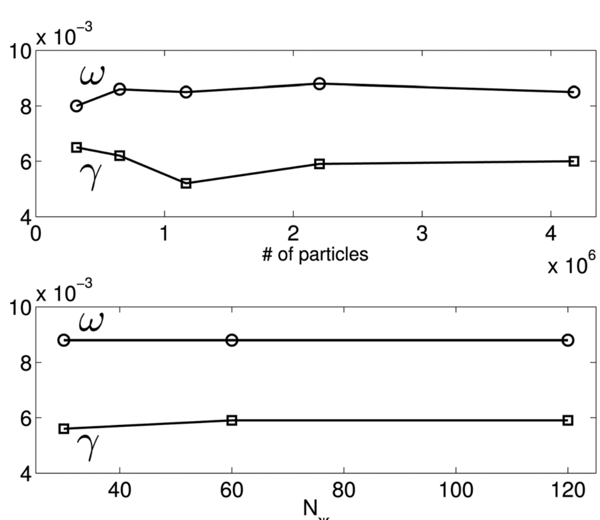

FIG. 8. Frequency $\omega(\circ)$ and growth rate γ ($\square$) convergence with respect to the number of particles (top panel) and the number of grid points in the radial direction N_ψ (bottom panel). 4-point gyro-averaging is used in the equations of motion and FLR effects are retained in force balance equation using spectral method.

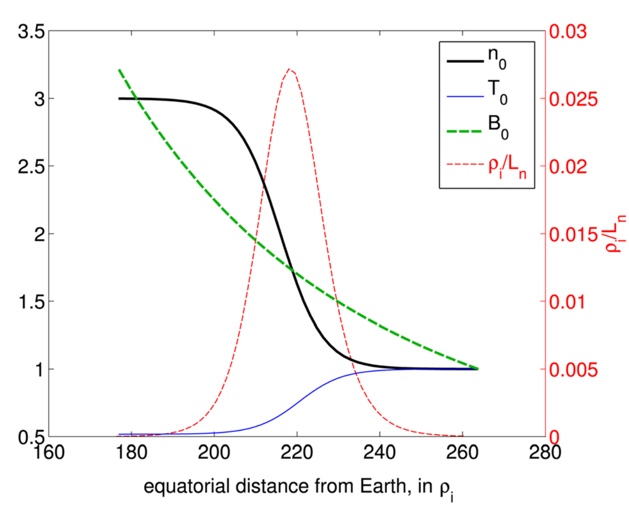

FIG. 10. (Color online) Density, temperature, and magnetic field profiles along the equator used in the simulation. Also plotted is the value of ρ_i/L_n (red, thin, interrupted line), where L_n is the density gradient scale length.

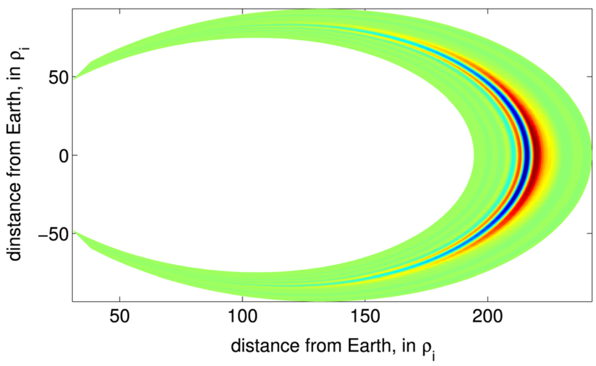

FIG. 11. (Color) Contour plot showing $\delta B_\parallel$ in the $\chi - \psi$ plane. The dark blue color designates the maximum negative amplitude, and the dark red color designates the maximum positive amplitude. 4-point gyro-averaging was used in the equations of motion and FLR effects were retained in force balance equation using spectral method.

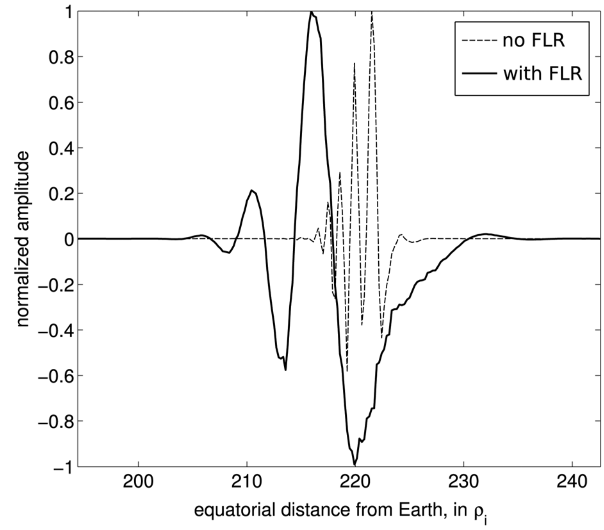

FIG. 13. Radial structure of $\delta B_\parallel$ obtained without taking into account the FLR effects in the simulation code (thin, interrupted line), and with the FLR effects (thick, solid line) taken into account. 4-point gyro-averaging was used in the equations of motion and FLR effects were retained in force balance equation using spectral method. The measurement was taken at the equator.

define the equilibrium density profile, were $r_{max} = 260.3\rho_i$, $\Delta r = 84\rho_i$, and $d = 1$.

The Larmor radius at $r_{\max}$, to which distances were normalized, was $\rho_i \approx 228$km, and the ion cyclotron frequency, which determines temporal normalization, was $\Omega_i \approx 4\text{s}^{-1}$. The mode structure along the magnetic field is symmetric about the equator. Figure 12 shows the structure more clearly, at the equatorial distance of around 222 ρ_i, which is the location with the largest amplitude in Fig. 11. 4-point gyro-averaging was used in the equations of motion, and FLR effects were retained in force balance equation using the Bessel function operators, as in Eq. (12), with $k_\psi \rho_i \approx 1.04$.

When gyrokinetic effects are artificially removed in the simulation code the radial structure changes significantly. This can be seen in Fig. 13 where the two simulation results are compared. The radial structure is much wider in the gyrokinetic case, with FLR effects, because the instability favors lower $k_\perp \rho_i$ and because the flux surfaces are coupled as a result of the finite Larmor radius. When the finite Larmor radius effects are ignored, the system is radially local, and the simulation results show radial structures whose variations are on the order of the grid cell size. The structure is independent of the grid cell size when the finite Larmor radius effects are taken into account. In order to emphasize the difference between these two cases, the simulation results shown in Fig. 13 used 220 grid points in the radial direction.

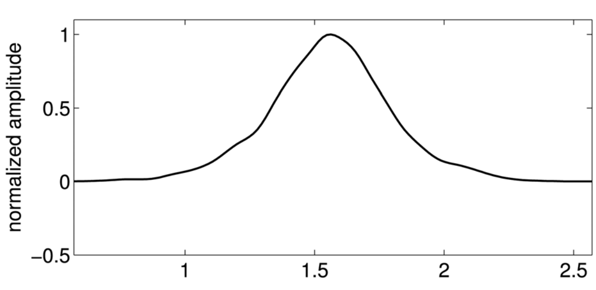

FIG. 12. Normalized structure of $\delta B_\parallel$ along the equilibrium magnetic field. The measurement was taken at the radial distance of around 222 ρ_i, where the Figure 11 shows a maximum amplitude. 4-point gyro-averaging was used in the equations of motion and FLR effects were retained in force balance equation using spectral method.

Figure 14 shows the time evolution of the radial structure along the equator. The structure was normalized at each time step to its maximum amplitude. The figure shows the instability emerging from random low amplitude noise, which is completely overcome at $2000\Omega_i^{-1}$. By comparison to Fig. 10, it can be seen that the location of the maximum amplitude as well as the width of the structure closely correspond to the location of maximum ω_* and the width of its profile. The time evolution contour plot further shows that the instability propagates radially away from its approximate region of excitation. The phase velocity towards the Earth is approximately $0.008v_{th}$, and away from the Earth it is approximately $0.014v_{th}$. As a reference, v_* at locations

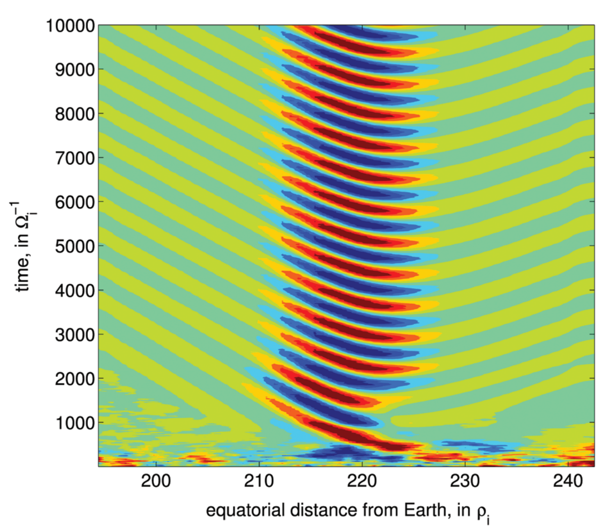

FIG. 14. (Color) Time evolution of the radial structure of $\delta B_\parallel$. The structure is normalized at each time step to its maximum value. 4-point gyro-averaging was used in the equations of motion and FLR effects were retained in force balance equation using spectral method. The measurement was taken at the equator.

$205.5\rho_i$, $219.5\rho_i$, and $235.6\rho_i$ was $0.0052v_{th}$, $0.0238v_{th}$, and $0.0037v_{th}$, respectively, and v_D at these locations was $0.0040v_{th}$, $0.0064v_{th}$, and $0.0093v_{th}$, respectively.

IV. SUMMARY

Steps taken in the development of the global, gyrokinetic, particle-in-cell simulation code in the dipole field of the Earth's magnetosphere were described. The purpose of the code is to investigate the compressional ultra low frequency (ULF) waves in the Earth's magnetosphere. Since the realistic magnetospheric equilibrium is complex and the full model of the compressional ULF waves involves multitude of physical processes, the Earth's magnetic field has been approximated by a dipole and the full physical model has been decomposed into simpler, verifiable components. The compressional component has been formulated in terms of the parallel magnetic perturbation $\delta B_\parallel$, and a numerical scheme has been devised for gyrokinetic simulations of low frequency compressional modes, in which gyro-averaging is performed explicitly in configuration space. The particle simulation code has been designed using the field-aligned flux coordinates for the magnetic dipole. The kinetic simulations were verified by modifying the equations of motion and the boundary conditions and running the simulations near the equator in order to approximate the slab limit in which analytic results are known. For the simplified drift-compressional model, a linear dispersion relation in the slab limit was found and solved using numerical Nyquist analysis. The verification process yielded satisfactory results, with small quantitative deviations from analytic results being attributed to the use of the dipole implementations to approximate a slab geometry. The first attempt to explore the predictive capabilities of the simulation code was focused on recovering the global field-aligned structure of the magnetic field perturbation of the drift-compressional mode and the finite-Larmor-radius (FLR) effects on frequency and growth rate. The field-aligned structure is seen to be symmetric about the equator, and the mode propagates in the direction of ion diamagnetic drift. However, it has been noted that for lower η values, the direction of propagation may change to be opposite of ion diamagnetic drift and the poloidal structure may become odd. This has also been observed when the $k_\perp\rho_i$ parameter was varied and will be further investigated. The scan on $k_\perp\rho_i$ showed that the growth rate tends to decrease as $k_\perp\rho_i$ increases, in agreement with the slab dispersion relation. Finding the radial structure requires accurately implementing the FLR effects. The results show that the radial structure is broadened when the FLR is taken into account. The location of the maximum amplitude of the structure and its width correspond to the location of maximum pressure gradient and the width of its profile, respectively. The instability propagates radially away from the region of excitation.

ACKNOWLEDGMENTS

This work was supported by National Science Foundation and U. S. Department of Energy grants. We gratefully acknowledge useful discussions with Alain Brizard, Liu Chen, Chris Crabtree, and Roger McWilliams. We also thank the referee whose meticulous review has helped improve this manuscript.

APPENDIX A: PARTICLE AND GYROCENTER DISTRIBUTION FUNCTIONS

The gyrokinetic Vlasov equation (1) describes the evolution of the gyrocenter distribution function F; however, the charge densities and currents which are required to solve the Poisson's equation and the Ampère's law are determined from the particle distribution function f using Eqs. (4) and (5). The relationship between the particle distribution function f and the gyrocenter distribution function F is $f(\mathbf{x},\mathbf{v},t) \equiv F[\mathbf{X}(\mathbf{x},\mathbf{v},t), v_\parallel(\mathbf{x},\mathbf{v},t), \mu(\mathbf{x},\mathbf{v},t), t]$, where $\mathbf{X}$ is the gyrocenter position vector, $v_\parallel$ is the gyrocenter parallel velocity, and μ is the magnetic moment, which is an adiabatic invariant. ξ, the gyro-angle, does not explicitly appear in F of Eq. (1), since the gyrokinetic Vlasov equation is constructed to govern the gyro-phase averaged distribution function. Following Ref. 11, the transformation equations from particle coordinates $\mathbf{z} \equiv (\mathbf{x},\mathbf{v})$ to guiding-center coordinates $\mathbf{Z}_0 \equiv (\mathbf{X}_0, v_{\parallel 0}, \mu_0, \xi_0)$ are, to lowest order in ρ/L_B,

$$X_0 = x - \rho, \quad v_{\parallel 0} = \widehat{\mathbf{b}}\cdot\mathbf{v}, \quad \mu_0 = mv_\perp^2/2B_0,$$
$$\xi_0 = \tan^{-1}(\widehat{\mathbf{e}}_1\cdot\mathbf{v}/\widehat{\mathbf{e}}_2\cdot\mathbf{v}), \tag{A1}$$

and from guiding-center to gyrocenter coordinates $\mathbf{Z} \equiv (\mathbf{X}, v_\parallel, \mu, \xi)$ are, to lowest order in perturbation amplitude,

$$\begin{aligned}
\mathbf{X} &= \mathbf{X}_0 + \delta\mathbf{A}_\perp \times \frac{\widehat{\mathbf{b}}}{B_0} - \frac{1}{m}\left(\frac{\widehat{\mathbf{b}}}{\Omega}\times\nabla_0\delta S + \widehat{\mathbf{b}}\frac{\partial\delta S}{\partial v_{\parallel 0}}\right),\\
v_\parallel &= v_{\parallel 0} + \frac{e\delta\tilde{A}_\parallel}{mc} + \frac{\widehat{\mathbf{b}}}{m}\cdot\nabla_0\delta S,\\
\mu &= \mu_0 + \frac{e^2}{mc^2}\left(\delta\mathbf{A}_\perp\cdot\frac{\partial\boldsymbol{\rho}}{\partial\xi_0}\right) + \frac{e}{mc}\frac{\partial\delta S}{\partial\xi_0},\\
\xi &= \xi_0 - \frac{e^2}{mc^2}\left(\delta\mathbf{A}_\perp\cdot\frac{\partial\boldsymbol{\rho}}{\partial\mu_0}\right) - \frac{e}{mc}\frac{\partial\delta S}{\partial\mu_0}.
\end{aligned} \tag{A2}$$

The definitions of various symbols are $v_\perp \equiv |\widehat{\mathbf{b}}\times(\mathbf{v}\times\widehat{\mathbf{b}})|$, $\boldsymbol{\rho} \equiv \Omega^{-1}\widehat{\mathbf{b}}\times\mathbf{v}_\perp = \rho_\perp(\widehat{\mathbf{e}}_1\cos\xi_0 - \widehat{\mathbf{e}}_2\sin\xi_0)$, $\Omega = eB_0/mc$, and the unit vector $\widehat{\mathbf{b}} = \widehat{\mathbf{e}}_1\times\widehat{\mathbf{e}}_2$ points along the equilibrium magnetic field at particle position. The 0 subscript designates the equilibrium component and δ the perturbed component. Tilde designates the gyro-angle dependent part of the field, thus $\delta\tilde{A}_\parallel \equiv \delta A_\parallel - \langle\delta A_\parallel\rangle$, where $\langle ... \rangle$ is the gyro-phase average. $\delta S(\mathbf{X}_0, v_{\parallel 0}, \mu_0, \xi_0, t)$ is sometimes called the phase-space gauge-function[13] (also see Ref. 31) or a generating function and is chosen to be the solution of $d\delta S/dt = e\delta\tilde{\psi}$, where $\delta\psi \equiv \delta\Phi - \delta\mathbf{A}\cdot(v_{\parallel 0}\widehat{\mathbf{b}} + \Omega\rho\times\widehat{\mathbf{b}})/c$. To lowest order $\delta S \equiv (e/\Omega)\int d\xi_0\delta\tilde{\psi}$. The field quantities $\delta\phi$ and $\delta\mathbf{A}$ are evaluated[11] at the particle position $\mathbf{x} = \mathbf{X}_0 + \boldsymbol{\rho}$ and therefore depend on the gyro-angle through $\boldsymbol{\rho}$.

The scalar invariance can be expanded to first order in perturbation amplitude δ as,

$$f_0(\mathbf{z}) + \delta f(\mathbf{z}, t) = F_0(\mathbf{Z}) + \delta F(\mathbf{Z}, t) \approx F_0(\mathbf{Z}_0) + \delta\mathbf{Z} \cdot \frac{\partial F_0}{\partial \mathbf{Z}_0} + \delta F(\mathbf{Z}_0, t). \quad \text{(A3)}$$

The $\delta\mathbf{Z}$ stands for the perturbed part of the transformation equations between gyrocenter coordinate and the guiding-center coordinates, i.e., $\delta\mathbf{Z} = \mathbf{Z} - \mathbf{Z}_0$.

Then, since $f_0(\mathbf{z}) = F_0(\mathbf{Z}_0)$,

$$\delta f(\mathbf{z}, t) \approx \delta\mathbf{Z} \cdot \frac{\partial F_0(\mathbf{Z}_0)}{\partial \mathbf{Z}_0} + \delta F(\mathbf{Z}_0, t). \quad \text{(A4)}$$

For F_0, the local Maxwellian distribution is used with weak spatial gradients in density and temperature. To lowest order, only the terms $\delta v_\parallel \frac{\partial F_0}{\partial v_\parallel}$ and $\delta\mu \frac{\partial F_0}{\partial \mu}$ survive. Explicitly,

$$\delta v_\parallel \frac{\partial F_0}{\partial v_\parallel} \approx -\frac{e v_\parallel}{Tc} F_0 \left(\delta A_\parallel - \langle \delta A_\parallel \rangle \right), \quad \text{(A5)}$$

$$\begin{aligned}\delta\mu \frac{\partial F_0}{\partial \mu} \approx -\frac{\Omega}{T} F_0 \frac{e}{c} \left(\delta \mathbf{A}_\perp \cdot \frac{\partial \boldsymbol{\rho}}{\partial \xi_0} \right) - \frac{e}{T} F_0 \Big\{ \delta\Phi - \langle \delta\Phi \rangle \\ - \left[\delta\mathbf{A} \cdot \left(v_{\parallel 0} \hat{\mathbf{b}} + \Omega \boldsymbol{\rho} \times \hat{\mathbf{b}} \right) \Big/ c \right. \\ \left. - \left\langle \delta\mathbf{A} \cdot \left(v_{\parallel 0} \hat{\mathbf{b}} + \Omega \boldsymbol{\rho} \times \hat{\mathbf{b}} \right) \Big/ c \right\rangle \right] \Big\}. \quad \text{(A6)}\end{aligned}$$

The first term of (A6) can be combined with the terms containing $\delta\mathbf{A} \cdot \Omega\boldsymbol{\rho} \times \hat{\mathbf{b}}$ using

$$\frac{\partial \boldsymbol{\rho}}{\partial \xi_0} = \frac{\mathbf{v}_\perp}{\Omega} \quad \text{(A7)}$$

and by rewriting

$$\delta\mathbf{A} \cdot \boldsymbol{\rho} \times \hat{\mathbf{b}} = \delta\mathbf{A} \cdot \frac{1}{\Omega} \left(\hat{\mathbf{b}} \times \mathbf{v}_\perp \right) \times \hat{\mathbf{b}}. \quad \text{(A8)}$$

The result is

$$\begin{aligned}\delta\mu \frac{\partial F_0}{\partial \mu} \approx -\frac{e}{T} F_0 \Big\{ \delta\Phi - \langle \delta\Phi \rangle - [\delta\mathbf{A} \cdot v_{\parallel 0} \hat{\mathbf{b}}/c \\ - \langle \delta\mathbf{A} \cdot v_{\parallel 0} \hat{\mathbf{b}}/c \rangle + \langle \delta\mathbf{A} \cdot \mathbf{v}_\perp / c \rangle] \Big\}. \quad \text{(A9)}\end{aligned}$$

Using (A9) and (A5) in (A4) results in (Ref. 12)

$$\begin{aligned}\delta f(\mathbf{x}, \mathbf{v}, t) \approx -\frac{e}{T} F_0 \{ \delta\Phi(\mathbf{x}, t) - \langle \delta\Phi(\mathbf{x}, t) \rangle \\ + \langle \delta\mathbf{A}(\mathbf{x}, t) \cdot \mathbf{v}_\perp / c \rangle \} + \delta F(\mathbf{Z}_0, t). \quad \text{(A10)}\end{aligned}$$

More rigorous discussion may be found in Refs. 11–13.

APPENDIX B: GYROKINETIC FIELD EQUATIONS

The following discusses the gyrokinetic field equations presented in Sec. II A in more detail. The gyrokinetic system contains the Poisson's equation, the parallel Ampère's law, and the perpendicular Ampère's law given by

$$\nabla_\perp^2 \delta\Phi = -4\pi \sum q \int d\mathbf{v} \delta f, \quad \text{(B1)}$$

$$\nabla_\perp^2 \delta A_\parallel = -4\pi \sum \frac{q}{c} \int d\mathbf{v} v_\parallel \delta f, \quad \text{(B2)}$$

$$\hat{\mathbf{b}} \times \nabla_\perp \delta B_\parallel = -4\pi \sum \frac{q}{c} \int d\mathbf{v} \mathbf{v}_\perp \delta f, \quad \text{(B3)}$$

respectively, where $\int d\mathbf{v} \equiv \int_0^{2\pi} \int_0^\infty \int_{-\infty}^\infty \frac{B_0}{m} dv_\parallel d\mu d\xi$ and the species index has been dropped for simplicity of presentation. Also, the 0 subscript has been dropped from the guiding-center variables $(\mathbf{X}_0, v_{\parallel 0}, \mu_0, \xi_0)$ in this section, since the gyrocenter variables will not explicitly appear because the phase space variables appearing in Eq. (6) are in the lowest order. With all components of the electromagnetic field kept and a locally nonuniform, bi-Maxwellian equilibrium distribution $F_0 = n_0(\mathbf{x}) \sqrt{m^3/(2\pi)^3 T_\parallel(\mathbf{x}) T_\perp(\mathbf{x})^2} e^{-m v_\parallel^2 / 2T_\parallel(\mathbf{x}) - \mu B_0(\mathbf{x}) / T_\perp(\mathbf{x})}$, Eq. (6) becomes

$$\begin{aligned}\delta f(\mathbf{x}, \mathbf{v}, t) = \delta F(\mathbf{Z}, t) - \frac{q}{T_\perp} F_0 (\delta\Phi(\mathbf{x}, t) - \langle \delta\Phi(\mathbf{x}, t) \rangle) \\ + \frac{q v_\parallel}{c T_\perp} F_0 (\delta A_\parallel(\mathbf{x}, t) - \langle \delta A_\parallel(\mathbf{x}, t) \rangle) \left(1 - \frac{T_\perp}{T_\parallel} \right) \\ - \frac{q}{c T_\perp} F_0 \langle \delta \mathbf{A}_\perp(\mathbf{x}, t) \cdot \mathbf{v}_\perp \rangle. \quad \text{(B4)}\end{aligned}$$

The various moments to be used in the field equations are then

$$\begin{aligned}\int d\mathbf{v} \delta f = \int d\mathbf{V} \delta F(\mathbf{Z}, t) + \frac{q}{T_\perp} \int d\mathbf{V} F_0 \langle \delta\Phi(\mathbf{x}, t) \rangle \\ - \frac{q}{T_\perp} n_0 \delta\Phi(\mathbf{r}, t) + \frac{1}{\rho_{th}^2 B_0} \int d\mathbf{V} F_0 \left\langle \int_0^\rho r dr \delta B_\parallel(\mathbf{x}, t) \right\rangle, \quad \text{(B5)}\end{aligned}$$

$$\begin{aligned}\int d\mathbf{v} v_\parallel \delta f = \int d\mathbf{V} v_\parallel \delta F(\mathbf{Z}, t) + \frac{q n_0}{cm} \frac{T_\parallel}{T_\perp} \Big(\delta A_\parallel(\mathbf{r}, t) \\ - \frac{m}{T_\parallel n_0} \int d\mathbf{V} v_\parallel^2 F_0 \langle \delta A_\parallel(\mathbf{x}, t) \rangle \Big) \left(1 - \frac{T_\perp}{T_\parallel} \right), \quad \text{(B6)}\end{aligned}$$

$$\begin{aligned}\int d\mathbf{v} \mathbf{v}_\perp \delta f = \Omega \hat{\mathbf{b}} \times \nabla \Big(\int d\mathbf{V} \int_0^\rho r dr \delta F(\mathbf{Z}, t) \\ + \frac{q}{T_\perp} \int d\mathbf{V} F_0 \int_0^\rho r dr \langle \delta\Phi(\mathbf{x}, t) \rangle \\ + \int d\mathbf{V} \int_0^\rho r dr \frac{F_0}{\rho_{th}^2 B_0} \left\langle \int_0^\rho r' dr' \delta B_\parallel(\mathbf{x}, t) \right\rangle \Big), \quad \text{(B7)}\end{aligned}$$

where $\int d\mathbf{V} = \int d^6\mathbf{Z} \frac{B_0}{m} \delta(\mathbf{r} - \mathbf{x}(\mathbf{Z}))$ and $\mathbf{r}$ is the position vector, $\rho_{th} = \sqrt{T_\perp/m}/\Omega$, and $\Omega = qB_0/mc$. The field equations, Eqs. (7) and (8), may then be written as

$$\begin{aligned}4\pi \sum q \Big\{ \frac{q}{T_\perp} \int d\mathbf{V} F_0 \langle \delta\Phi(\mathbf{x}, t) \rangle - \frac{q}{T_\perp} n_0 \delta\Phi(\mathbf{r}, t) \\ + \frac{1}{\rho_{th}^2 B_0} \int d\mathbf{V} F_0 \left\langle \int_0^\rho r dr \delta B_\parallel(\mathbf{x}, t) \right\rangle \Big\} \\ = -4\pi \sum q \int d\mathbf{V} \delta F(\mathbf{Z}, t), \quad \text{(B8)}\end{aligned}$$

$$\nabla_\perp^2 \delta A_\parallel(\mathbf{r},t) + 4\pi \sum \frac{q}{c}\left\{ \frac{qn_0}{cm}\frac{T_\parallel}{T_\perp}\left[\delta A_\parallel(\mathbf{r},t) - \frac{m}{T_\parallel n_0}\int d\mathbf{V} v_\parallel^2 F_0 \left\langle \delta A_\parallel(\mathbf{x},t)\right\rangle\right]\left(1-\frac{T_\perp}{T_\parallel}\right)\right\} = -4\pi\sum\frac{q}{c}\int d\mathbf{V} v_\parallel \delta F(\mathbf{Z},t), \quad \text{(B9)}$$

$$\frac{\delta B_\parallel(\mathbf{r},t)B_0}{4\pi} + \sum\frac{q}{c}\Omega B_0\left\{\frac{q}{T_\perp}\int d\mathbf{V}F_0\int_0^\rho rdr\langle\delta\Phi(\mathbf{x},t)\rangle + \int d\mathbf{V}\int_0^\rho rdr\frac{F_0}{\rho_{th}^2 B_0}\left\langle\int_0^\rho r'dr'\delta B_\parallel(\mathbf{x},t)\right\rangle\right)\right\} = -\sum\frac{q}{c}\Omega B_0\int d\mathbf{V}\int_0^\rho rdr\delta F(\mathbf{Z},t). \quad \text{(B10)}$$

The quasineutrality condition has been assumed in deriving Eq. (B8), and the assumption of weak equilibrium gradient scale length has been used to remove the operator $\hat{\mathbf{b}}\times\nabla$ in Eq. (B10). The phase space integrals in Eqs. (B8)–(B10) are over the particle phase space; however, δF and the gyro-averaged quantities are functions of the guiding-center coordinates $(\mathbf{X}, v_\parallel, \mu)$, to lowest order. The difference between the evaluations of δF in guiding-center instead of gyrocenter coordinates contributes terms of higher order not retained within the system. When performing the phase space integration it is important to take into account the difference between the guiding-center position $\mathbf{X}$ and the particle position $\mathbf{x}$. The transformations between guiding-center and particle coordinates are commonly represented by operators $e^{\rho\cdot\nabla}$ which enable obtaining formal analytic expressions for the field equations in terms of Bessel functions. This step has not been taken in Eqs. (B8)–(B10), since in particle simulations the gyro-orbit and gyro-surface averages are performed explicitly in configuration space by taking averages of the field quantities along the gyro-orbit or the surface enclosed by it, respectively.[15,20] The Poisson's equation (B8), the parallel Ampère's law (B9), and the low frequency perpendicular force balance equation (B10) may be solved in configuration space by combining the methods described in Refs. 15, 20, 21.

For purely compressional perturbations, the use of $v_\parallel$ formulation was motivated by the fact that unlike a formulation which uses energy as one of its coordinates, it does not contain ∂_t in the equations of motion. In addition, when the shear component of the magnetic field is included in the model, the "cancellation problem"[32,33] in the parallel Ampère's is avoided by using $v_\parallel$ instead of $p_\parallel$ formulation. However, in this case the equation of motion for $v_\parallel$, Eq. (3), contains the electromagnetic component of the parallel electric field, $-c^{-1}\partial_t A_\parallel$. The numerical difficulties associated with this term, as well as the Courant condition for the streaming electrons in the parallel direction, may be avoided using the fluid-kinetic hybrid electron model.[34] In the model, an effective potential Ψ is defined by $\hat{\mathbf{b}}\cdot\nabla\Psi = \hat{\mathbf{b}}\cdot\nabla\delta\Phi + c^{-1}\partial_t\delta A_\parallel$ and used together with $\delta\Phi$ in the equations of motion instead of $-\partial_t\delta A_\parallel$. The fluid-kinetic hybrid electron model solves for electron dynamics order by order in the adiabatic expansion. To lowest order then $e\Psi/T_e = \delta n_e/n_0$.

The bi-Maxwellian distribution introduces the drift-mirror instability.[5] The mirror instability threshold condition may be derived using the slab model of Sec. III C, which now yields the dispersion relation

$$1+\frac{\beta_\perp}{(k_\perp\rho_i)^2}\left\{\left[\omega-\omega_*\left(1-\frac{1}{2}\left[\eta_\parallel+2\eta_\perp\right]\right)\right]K_1-\omega_*\eta_\perp K_2 + \omega_*\left(\eta_\perp-\eta_\parallel\right)K_3 + A\sqrt{2}v_{ti}k_\parallel K_4\right\}=0, \quad \text{(B11)}$$

where $A = T_\perp/T_\parallel - 1$, $v_{ti}^2 = T_\parallel/m$, $\eta_\parallel = \frac{\partial_\psi \ln T_\parallel(x)}{\partial_\psi \ln n_0(x)}$, $\eta_\perp = \frac{\partial_\psi \ln T_\perp(x)}{\partial_\psi \ln n_0(x)}$ and

$$K_3 = \frac{1}{\sqrt{\pi}}\int_0^\infty\int_{-\infty}^\infty \frac{\xi^2\epsilon J_1^2(\sqrt{2}k_\perp\rho_i\sqrt{\epsilon})d\xi d\epsilon}{\omega-\epsilon\omega_D-\xi\sqrt{2}v_{ti}k_\parallel}, \quad \text{(B12)}$$

$$K_4 = \frac{1}{\sqrt{\pi}}\int_0^\infty\int_{-\infty}^\infty \frac{\xi\epsilon J_1^2(\sqrt{2}k_\perp\rho_i\sqrt{\epsilon})d\xi d\epsilon}{\omega-\epsilon\omega_D-\xi\sqrt{2}v_{ti}k_\parallel}, \quad \text{(B13)}$$

with other symbols defined in Sec. III C. For $\omega_* = \omega_D = 0$ and $k_\perp\rho_i = 0$, the dispersion relation becomes $\xi Z(\xi) = (1-A\beta_\perp)/(1+A)/\beta_\perp$, where $\xi = \omega/\sqrt{2}v_{ti}k_\parallel$ and $Z(\xi)$ is the plasma dispersion function. In the limit $|\xi| \ll 1$, to lowest order, the real frequency is $\omega = 0$ and $\gamma = (A\beta_\perp - 1)/(1+A)/\beta_\perp$, giving the mirror instability threshold condition[35] $\beta_\perp(T_\perp/T_\parallel - 1) > 1$.

[1] X. Zhu and M. G. Kivelson, J. Geophys. Res. **96**, 19451 (1991).
[2] K. Takahashi, P. R. Higbie, and D. N. Baker, J. Geophys. Res. **90**, 1473, doi:10.1029/JA090iA02p01473 (1985).
[3] K. Takahashi, J. F. Fennell, E. Amata, and P. R. Higbie, J. Geophys. Res. **92**, 5857, doi:10.1029/JA092iA06p05857 (1987).
[4] K. Takahashi, Adv. Space Res. **8**, 427 (1988).
[5] A. Hasegawa, Phys. Fluids **12**, 2642 (1969).
[6] H. Qu, Z. Lin, and L. Chen, Geophys. Res. Lett. **35**, L10108, doi:10.1029/2008GL033907 (2008).
[7] L. Chen and B. Xu, AGU Fall Meeting Abstracts, **B9** (2002).
[8] M. N. Rosenbluth, Phys. Rev. Lett. **46**, 1525 (1981).
[9] C. Crabtree, W. Horton, H. V. Wong, and J. W. Van Dam, J. Geophys. Res. **108**, 1084, doi:10.1029/2002JA009555 (2003).
[10] C. Crabtree and L. Chen, Geophys. Res. Lett. **31**, L17804, doi:10.1029/2004GL020660 (2004).
[11] A. J. Brizard, Phys. Fluids B **4**, 1213 (1992).
[12] A. J. Brizard and T. S. Hahm, Rev. Mod. Phys. **79**, 421 (2007).
[13] A. J. Brizard, J. Plasma Phys. **41**, 541 (1989).
[14] L. Chen and A. Hasegawa, J. Geophys. Res. **96**, 1503, doi:10.1029/90JA02346 (1991).
[15] P. Porazik and Z. Lin, Commun. Comput. Phys. **10**, 899 (2011).
[16] W. Tang, J. Connor, and R. Hastie, Nucl. Fusion **20**, 1439 (1980).
[17] Y. Lin, X. Wang, Z. Lin, and L. Chen, Plasma Physics Controlled Fusion **47**, 657 (2005).
[18] T. S. Hahm, L. Wang, and J. Madsen, Phys. Plasmas **16**, 022305 (2009).
[19] H. Qin, W. M. Tang, W. W. Lee, and G. Rewoldt, Phys. Plasmas **6**, 1575 (1999).
[20] W. W. Lee, J. Comput. Phys. **72**, 243 (1987).
[21] Z. Lin and W. W. Lee, Phys. Rev. E **52**, 5646 (1995).
[22] Y. L. Al'pert, *The Near-Earth and Interplanetary Plasma* (Cambridge University Press, Cambridge, 1983).
[23] D. P. Stern, J. Geophys. Res. **99**, 17169, doi:10.1029/94JA01239 (1994).
[24] A. A. Chan, "Interaction of Energetic Ring Current Protons With Magnetospheric Hydromagnetic Waves," Ph.D. thesis (Princeton University, 1991).
[25] S. I. Krasheninnikov, P. J. Catto, and R. D. Hazeltine, Phys. Rev. Lett. **82**, 2689 (1999).

[26]R. Hastie, J. Taylor, and F. A. Haas, Ann. Phys. **41**, 302 (1967).
[27]Z. Lin, T. S. Hahm, W. W. Lee, W. M. Tang, and R. B. White, Science **281**, 1835 (1998).
[28]C. K. Birdsall and A. B. Langdon, *Plasma Physics Via Computer Simulation* (Institute of Physics Publishing, New York, NY, 1991).
[29]S. E. Parker and W. W. Lee, Phys. Fluids B **5**, 77 (1993).
[30]G. Hu and J. A. Krommes, Phys. Plasmas **1**, 863 (1994).
[31]R. G. Littlejohn, J. Plasma Phys. **29**, 111 (1983).
[32]Y. Chen and S. Parker, Phys. Plasmas **8**, 2095 (2001).
[33]A. Mishchenko, R. Hatzky, and A. Konies, Phys. Plasmas **11**, 5480 (2004).
[34]Z. Lin and L. Chen, Phys. Plasmas **8**, 1447 (2001).
[35]R. M. Kulsrud, *Handbook of Plasma Physics* (North-Holland Publishing Company, Amsterdam, Netherlands, 1983).